Stabilizing multiple topological fermions on a quantum computer (supplementary information)

Jin Ming Koh,[1,*] Tommy Tai,[2] Yong Han Phee,[3] Wei En Ng,[3,4] and Ching Hua Lee[3,†]

[1] *Division of Physics, Mathematics and Astronomy, California Institute of Technology, Pasadena, California 91125, United States*
[2] *Cavendish Laboratory, University of Cambridge, JJ Thomson Ave, Cambridge CB3 0HE, United Kingdom*
[3] *Department of Physics, National University of Singapore, Singapore 117542*
[4] *School of Computing, National University of Singapore, Singapore 117417*

Supplementary Note 1. PHYSICAL MODELS

A. Single-particle topology: Su-Schrieffer-Heeger (SSH) model and extended Kitaev chain (KC)

We first review the symmetry-protected topological (SPT) phases realized in this work. In general, SPT phases are gapped phases protected by at least one global symmetry—for example time reversal, charge conjugation or crystalline symmetry [1–4]. In the recent decades, the study of SPT phases has been greatly fueled by the discovery of topological insulators, topological superconductors and topological semimetals [5–8]. Each topological phase is characterized by at least one topologically invariant quantity. A topological phase transition occurs when this invariant changes upon varying any of the parameters of the system. The simplest of such invariants takes the form of winding numbers in momentum space, as we shall describe below.

In this work, we consider the BDI- and D-class SPT phases in 1D, which are characterized by topological invariants that are defined at the level of single particle states. Our phases are realized via the extended Kitaev chain (KC) model, which encompasses the BDI class with $\mathbb{Z}$ invariant, as epitomized by the well-known Su-Schrieffer-Heeger (SSH) model, and a less well-known D class with $\mathbb{Z}_2$ topological invariant.

The archetypal Su-Schrieffer–Heeger (SSH) model takes the form of a spinless Hermitian chain with two sublattice sites A and B per unit cell [7, 9–12]. This model has been extensively realized in various platforms, particularly classical ones [12–16]. The inter-site hopping depends on whether the sites are in the same sublattice or not:

$$H^{\mathrm{SSH}} = \sum_{j=1}^{N} v c_j^\dagger d_j + \sum_{j=1}^{N-1} w d_j^\dagger c_{j+1} + \mathrm{h.c.}, \tag{1}$$

for a chain with N unit cells under open boundary conditions (OBCs), with intracell and intercell hopping coefficients v and w respectively. When $|w| > |v|$, this chain supports topologically robust edge states with zero eigenenergies, as can be intuitively visualized in a mechanics setting [17]. To understand this topological robustness mathematically, we expand H^{SSH} in the Pauli basis, such that it takes the form of a 3-vector $\mathbf{h}(k)$ in momentum space:

$$H^{\mathrm{SSH}}(k) = \mathbf{h}(k)\cdot\boldsymbol{\sigma} = h_x(k)\sigma^x + h_y(k)\sigma^y + h_z(k)\sigma^z, \tag{2}$$

where $\mathbf{h}(k)$ traces a closed loop due to the periodicity of lattice momentum k. Importantly, due to the sublattice symmetry characteristic of the BDI class, $h_z(k) = 0$ and $\mathbf{h}(k)$ is restricted to a 2D plane. Its topology is hence classified by the first homotopy group $\mathbb{Z}$ of a punctured plane, *i.e.* the number of times $\mathbf{h}(k)$ encircles the origin, which is nonzero when the chain is topologically non-trivial.

To motivate the parent model we used in this work, namely the extended Kitaev chain (KC), we note that the SSH model is mathematically equivalent to the simple Kitaev chain (SKC) developed for explaining Majorana zero modes in topological superconductivity [18]. In its original form, its Hamiltonian contains hopping terms (t) and Bogoliubov-de Gennes pairing (Δ) terms between adjacent sites, as well as on-site chemical potential (μ) terms:

$$H^{\mathrm{SKC}} = \sum_j \left[t\left(\eta_j^\dagger \eta_{j+1} + \eta_{j+1}^\dagger \eta_j\right) + \Delta\left(\eta_j^\dagger \eta_{j+1}^\dagger + \eta_{j+1}\eta_j\right)\right] + \mu \sum_j \eta_j^\dagger \eta_j, \tag{3}$$

* jkoh@caltech.edu

† phylch@nus.edu.sg

where $\eta^\dagger, \eta$ creates/annihilates the Bogoliubov-de Gennes quasiparticles. It can be shown via a Bogoliubov transformation to the c, d operators that H^{SKC} is unitarily equivalent to the SSH chain [19], with the chemical potential term corresponding to an effective coupling between the two SSH sublattices [20]. Importantly, SSH topological boundary modes correspond to highly sought-after Majorana zero modes at the ends of these chains, whose potential application in fault-tolerant quantum computing has led to intense investigations [21–24], and Ref. [25] for D class.

By introducing next nearest neighbour (NNN) hoppings and pairings [26, 27], this model can be generalized into an *extended* Kitaev chain model with versatile topological properties. In the basis containing sublattices A and B, the Hamiltonian takes the form

$$\begin{aligned} H^{\mathrm{KC}} = \mu \sum_{j=1}^{N} \left(c_j^\dagger c_j - d_j^\dagger d_j \right) + \frac{v_1}{2} \sum_{j=1}^{N-1} \left(c_j^\dagger c_{j+1} - d_j^\dagger d_{j+1} + \mathrm{h.c.} \right) + \frac{v_2}{2} \sum_{j=1}^{N-2} \left(c_j^\dagger c_{j+2} - d_j^\dagger d_{j+2} + \mathrm{h.c.} \right) \\ + \frac{i\Delta_2 \sin\phi}{2} \sum_{j=1}^{N-2} \left(c_j^\dagger d_{j+2} + d_j^\dagger c_{j+2} - \mathrm{h.c.} \right) + \frac{\Delta_2 \cos\phi}{2} \sum_{j=1}^{N-2} \left(d_j^\dagger c_{j+2} - c_j^\dagger d_{j+2} + \mathrm{h.c.} \right) \\ + \frac{\Delta_1}{2} \sum_{j=1}^{N-1} \left(d_j^\dagger c_{j+1} - c_j^\dagger d_{j+1} + \mathrm{h.c.} \right), \end{aligned} \tag{4}$$

where operators c_j, d_j respectively act on the A- and B-sites of the j-th unit cell. Removing NNN hoppings, phases and pairings ($v_2 = \phi = \Delta_2 = 0$) recovers the standard 2-band Kitaev chain (SKC), or equivalently the SSH model. In momentum space, Eq. (4) takes the form [26] $H^{\mathrm{KC}}(k) = \mathbf{h}^{\mathrm{KC}} \cdot \boldsymbol{\sigma}$:

$$\begin{aligned} h_x^{\mathrm{KC}}(k) &= \Delta_2 \sin\phi \sin 2k, \\ h_y^{\mathrm{KC}}(k) &= \Delta_2 \cos\phi \sin 2k + \Delta_1 \sin k, \\ h_z^{\mathrm{KC}}(k) &= \mu - v_1 \cos k - v_2 \cos 2k. \end{aligned} \tag{5}$$

The competition between nearest neighbour and next nearest neighbour terms results in a richer phase diagram, supporting up to two topological zero modes at each end. These topological modes are evident in the bandstructure. Notably, when ϕ is not a multiple of π, all three components of $\mathbf{h}^{\mathrm{KC}}$ are nonzero, and the KC model possesses D-class symmetry characterized by a $\mathbb{Z}_2$ topological invariant, according to the ten-fold-way classification [5, 28]. But when ϕ is a multiple of π, $h_x^{\mathrm{KC}}(k)$ vanishes, and the model only belongs to the BDI class characterized by a $\mathbb{Z}$ topological invariant, the same as the SSH model. In the winding number perspective, the topological invariant of the BDI class is the number of times $\mathbf{h}(k)$ encircle the origin. Again, when ϕ is a multiple of π, $\mathbf{h}(k)$ is constrained to a plane. However, when ϕ is not a multiple of π, $\mathbf{h}(k)$ traces out a closed path on a unit sphere. While there is no longer a well-defined winding around the origin, the path still possesses chiral symmetry which forces its k and $-k$ paths to be related. The geometric interpretations of its two $\mathbb{Z}_2$ classes are elaborated in Refs. [29] and [30], albeit in a more general non-Hermitian context.

We note that all Hamiltonians considered in our work conserves total particle number as a symmetry, that is,

$$\left[H^{\mathrm{KC}}, O\right] = \left[H^{\mathrm{SSH}}, O\right] = 0, \qquad O = \sum_{j=1}^{N} \left(c_j^\dagger c_j + d_j^\dagger d_j \right), \tag{6}$$

hence enabling our use of post-selection on particle number (see Supplementary Note 3 C 2).

B. Idealized Edge Modes

Under certain extreme parameter limits, the topological edge mode wavefunctions of H^{SSH} and H^{KC} take particularly simple forms. We refer to these as idealized edge states. The robustness conferred by their SPT nature means that away from these limits, topological edge modes still possess strong overlap with these idealized ones, so long as the system remains in the same topological phase. These idealized states were included in Table I of the main text; they are most conveniently given in the form $|\alpha\rangle = c[\alpha]^\dagger |\mathrm{vac}\rangle$ for creation operator $c[\alpha]^\dagger$ and vacuum state $|\mathrm{vac}\rangle = |000\ldots\rangle$.

The idealized edge states $|1_1^{\mathrm{L,R}}\rangle$ of the $\gamma = \pi$ phase of D-class H^{KC} are identical to those of the BDI-class H^{KC}, which makes them redundant to investigate. From the 1-particle $|\alpha\rangle$ of our models, 2-particle idealized states can be constructed by sequentially applying the operators of *different* 1-particle state—due to Pauli exclusion, we cannot

Model	Regime	Parameter Limit
H^{SSH}	$\nu = 1$	$v/w \to 0$
H^{KC} (BDI-Class)	$\nu = 1$	$\mu, t_2, \Delta_2, \phi \to 0,\ t_1 = \Delta_1$
	$\nu = 2$	$\mu, t_1, \Delta_1, \phi \to 0,\ t_2 = \Delta_2$
H^{KC} (D-Class)	$\gamma = \pi$	$\mu, t_2, \Delta_2 \to 0,\ t_1 = \Delta_1$
	$\gamma = 0$	$\mu, t_1, \Delta_1 \to 0,\ t_2 = \Delta_2$

Supplementary Table 1. Summary of extreme parameter limits of H^{SSH} and H^{KC}.

have 2 particles in the same state. For example, $|2_{12}^{\mathrm{LR}}\rangle = c[1_1^{\mathrm{L}}]^\dagger c[1_2^{\mathrm{R}}]^\dagger |\mathrm{vac}\rangle$. The extreme parameter limits for our models are summarized in Supplementary Table 1. One can verify the $|\alpha\rangle$ listed above by checking that the associated number operators are symmetries of the corresponding Hamiltonians $H \in \{H^{\mathrm{SSH}}, H^{\mathrm{KC}}\}$ in the parameter limits,

$$\big[H, c[\alpha]^\dagger c[\alpha]\big] = 0, \tag{7}$$

which means their occupancy profiles are conserved throughout time-evolution.

Supplementary Note 2. QUANTUM COMPUTING PRELIMINARIES

We provide a brief introduction to quantum computing and simulation, and to the IBM Q platform [31–34] through which we run experiments on quantum hardware. The IBM Q platform is accessible through the cloud—in fact a number of machines are freely available for public use—and has been utilized in a considerable number of studies since launch [35–44]. To set the technical context for our methods, which are detailed in the Methods section of the main text, we discuss certain specifics of quantum computing in relation to the IBM Q platform; we point readers to other articles for a more general overview [45–48].

A. IBM Q Platform

We describe the workflow of running experiments on IBM Q, whose details, in particular the construction of quantum circuits and the readout of measurement results, are relevant to our computation methods; though the concepts are broadly general. One uses the *Qiskit* API [33, 34] on Python to define quantum circuits and submit them to IBM Q backends (machines) for execution; the backend then reports raw measurement results, which can be processed to recover expectation values, correlation functions, and other quantities of interest. The backends execute the submitted experiments asynchronously in a fairshare queuing system. We use a group of QV-32 backends, namely *ibmq_paris* (27 qubits), *ibmq_toronto* (27 qubits), *ibmq_manhattan* (65 qubits), and *ibmq_guadalupe* (16 qubits), and the QV-16 backend *ibmq_boeblingen* (20 qubits). The quantum volume (QV) can be treated as a rough indicator of the overall capability of the machine—number of qubits, gate error rates, and decoherence times [49, 50]. These are the highest-volume machines accessible to the authors at the time of writing. To provide a ballpark measure of performance, the relaxation time T_1, that is the timescale of thermal decay of a qubit from the $|1\rangle$ state to the $|0\rangle$ state, and the dephasing time T_2, that is the timescale over which phase information of a qubit is lost, ranges $60\,\mu\mathrm{s} \leq T_1 \approx T_2 \leq 120\,\mu\mathrm{s}$ on average for these machines; and typical gate time is $T_{\mathrm{g}} \approx 420\,\mathrm{ns}$. Typical single-qubit ($\sqrt{X}$) gate error is $\mathcal{O}(10^{-3})$, and typical two-qubit (CX) gate error is $\mathcal{O}(10^{-2})$. An illustration of qubit layout is provided in Supplementary Figure 2.

B. Quantum Gates & Circuits

Current IBM Q hardware use transmon qubits [31–33] on cryogenic chips. Just as classical logic gates operate on bits, quantum gates operate on qubits. First, we define the computational basis,

$$|0\rangle = \begin{bmatrix} 1 \\ 0 \end{bmatrix}, \qquad |1\rangle = \begin{bmatrix} 0 \\ 1 \end{bmatrix}, \tag{8}$$

and the multi-qubit state notation $|x_1 x_2 \ldots x_n\rangle$ is shorthand for $|x_1\rangle \otimes |x_2\rangle \otimes \ldots \otimes |x_n\rangle$, where $\otimes$ is the tensor product. Note that the qubits are always distinguishable, unlike the logical fermions that they can represent. The single-qubit

Pauli gates are

$$\sigma^x = X = \begin{bmatrix} 0 & 1 \\ 1 & 0 \end{bmatrix}, \qquad \sigma^y = Y = \begin{bmatrix} 0 & -i \\ i & 0 \end{bmatrix}, \qquad \sigma^z = Z = \begin{bmatrix} 1 & 0 \\ 0 & -1 \end{bmatrix}, \tag{9}$$

which flip a qubit around the x-, y-, and z- axes of the Bloch sphere. For instance, the X gate is understood as the quantum analogue of the NOT classical gate, since $X|0\rangle = |1\rangle$ and $X|1\rangle = |0\rangle$. Generated from the Pauli gates are the rotation gates

$$\begin{aligned} R^x(\theta) &= e^{-i\theta\sigma^x/2} = \begin{bmatrix} \cos(\theta/2) & -i\sin(\theta/2) \\ -i\sin(\theta/2) & \cos(\theta/2) \end{bmatrix}, \\ R^y(\theta) &= e^{-i\theta\sigma^y/2} = \begin{bmatrix} \cos(\theta/2) & -\sin(\theta/2) \\ \sin(\theta/2) & \cos(\theta/2) \end{bmatrix}, \\ R^z(\theta) &= e^{-i\theta\sigma^z/2} = \begin{bmatrix} e^{-i\theta/2} & 0 \\ 0 & e^{i\theta/2} \end{bmatrix}. \end{aligned} \tag{10}$$

Other commonly used gates are the Hadamard, root-X and S gates,

$$H = \frac{1}{\sqrt{2}}\begin{bmatrix} 1 & 1 \\ 1 & -1 \end{bmatrix}, \qquad \sqrt{X} = \frac{1}{2}\begin{bmatrix} 1+i & 1-i \\ 1-i & 1+i \end{bmatrix}, \qquad S = \sqrt{Z} = \begin{bmatrix} 1 & 0 \\ 0 & i \end{bmatrix}. \tag{11}$$

The H gate is useful as it creates superpositions, in that $H|0\rangle = |+\rangle = (|0\rangle + |1\rangle)/\sqrt{2}$ and $H|1\rangle = |-\rangle = (|0\rangle - |1\rangle)/\sqrt{2}$, which are orthogonal on the equator of the Bloch sphere. That is, it shifts between the computational basis (z-basis) and the x-basis $|\pm\rangle$, which is also the single-qubit Fourier basis. All of these gates can be represented as special cases of the U_3 general single-qubit gate,

$$U_3(\theta,\phi,\lambda) = \begin{bmatrix} \cos(\theta/2) & -e^{i\lambda}\sin(\theta/2) \\ e^{i\phi}\sin(\theta/2) & e^{i(\phi+\lambda)}\cos(\theta/2) \end{bmatrix}. \tag{12}$$

Analogous to the U_3 gate, there are more restrictive U_1 and U_2 gates,

$$U_2(\phi,\lambda) = U_3(\pi/2,\phi,\lambda) = \frac{1}{\sqrt{2}}\begin{bmatrix} 1 & -e^{i\lambda} \\ e^{i\phi} & e^{i(\phi+\lambda)} \end{bmatrix}, \qquad U_1(\lambda) = U_3(0,0,\lambda) = \begin{bmatrix} 1 & 0 \\ 0 & e^{i\lambda} \end{bmatrix}, \tag{13}$$

which may allow lower error and faster execution time on quantum hardware. Indeed, on some IBM Q machines [33], U_1 gates are performed with software frame changes and therefore take negligible gate time; U_2 gates require frame changes and a single microwave pulse; and U_3 gates require two pulses. Since all operations are unitary, those that are also Hermitian are their own inverses; they are involutory. For example, $X^2 = Y^2 = Z^2 = H^2 = I$.

We now discuss multi-qubit gates. Of relevance is the controlled-U gate, which applies unitary U to a target qubit if the control qubit is $|1\rangle$. For two qubits,

$$\mathrm{CU}_{12} = \begin{bmatrix} I & 0 \\ 0 & U \end{bmatrix} = \begin{bmatrix} 1 & 0 & 0 & 0 \\ 0 & 1 & 0 & 0 \\ 0 & 0 & U_{11} & U_{12} \\ 0 & 0 & U_{21} & U_{22} \end{bmatrix}, \qquad \mathrm{CU}_{21} = \begin{bmatrix} 1 & 0 & 0 & 0 \\ 0 & U_{11} & 0 & U_{12} \\ 0 & 0 & 1 & 0 \\ 0 & U_{21} & 0 & U_{22} \end{bmatrix}, \tag{14}$$

where the first and second indices refer to the control and target qubits respectively. Setting $U = X$ gives the controlled-NOT (CNOT) gates, CX_{12} and CX_{21}, which are the entangling gates on IBM Q hardware. In general, for n qubits, the controlled unitary can be written

$$\mathrm{CU}_{ij} = |0\rangle_i \langle 0|_i \otimes I_j + |1\rangle_i \langle 1|_i \otimes U_j = \bigotimes_{k=1}^{n} (|0\rangle\langle 0|)^{\delta_{ik}} + \bigotimes_{k=1}^{n} (|1\rangle\langle 1|)^{\delta_{ik}} U^{\delta_{jk}}, \tag{15}$$

where padding with identity matrices on all other qubits $k \neq i, j$ is implicit for the left expression. We likewise extend Pauli gates to multi-qubit systems by padding over the remaining qubits,

$$\sigma_j^\mu = I_{2^{j-1}} \otimes \sigma^\mu \otimes I_{2^{n-j}}, \qquad \mu \in \{x, y, z\}. \tag{16}$$

A quantum circuit [45, 48] represents a series of gate operations on qubits. Wires in quantum circuits represent qubits, and time flows from the left to the right. The gates specified on the circuit are applied to the qubits in order—note, for sake of clarity, that this implies a reversal of the ordering of gates when written. For instance, $XYZ|\psi_0\rangle$

means gates Z acts on $|\psi_0\rangle$, followed by Y then X. It is standard convention that qubits are initialized to $|0\rangle$ at the start of a circuit. For organizational purposes, qubits may be grouped into registers. In *Qiskit*, quantum circuits comprise quantum registers each containing a number of qubits, and classical registers to which measurement results on qubits are written [33, 34]. Quantum measurements are discussed in Supplementary Note 2 C.

In principle, one is free to add arbitrary gates to a circuit—arbitrary unitaries spanning numerous qubits. However, digital quantum computers are engineered to support only a handful of basis gates. For example, IBM Q machines support $\{U_1, U_2, U_3, \mathrm{CX}\}$; in January 2021 some machines have switched to the $\{R^z, \sqrt{X}, X, \mathrm{CX}\}$ basis set [33]. These basis sets are universal, which allows arbitrary unitaries to be approximated to any desired precision. However, while the optimal decompositions for general one- and two-qubit unitaries are known, the latter through the KAK decomposition [51, 52], the optimal decomposition for n-qubit unitaries is not fully known and non-trivial to work out [53–56]. Finding circuit implementations of desired unitaries is a key challenge in programming digital quantum computers—it is for this purpose that trotterization and circuit recompilation techniques are used (see Supplementary Note 3 B). We note the decomposition $U_3(\theta, \phi, \lambda) = R^z(\phi + \pi)\sqrt{X}R^z(\theta + \pi)\sqrt{X}R^z(\lambda)$ up to global phase, hence our circuit ansatz for recompilation, represented using U_3 gates, can be equivalently applied for both of the IBM Q basis sets.

C. Measurements

All measurements are performed in the computational basis, that is, the measured observable is σ_i^z on qubit $i \in \mathbb{N}$. A value of 1 is written to the designated classical bit if a qubit state of $|1\rangle$ is projectively measured; and a value of 0 is written if $|0\rangle$ is measured [33, 34]. Since the results of quantum measurements are probabilistic, to obtain statistical estimates of expectation values many repetitions have to be performed—IBM Q enables each circuit to be run for a number of shots n_s to facilitate this. At the termination of the circuit, the bit values in the classical registers are concatenated into a measurement *bitstring*; the backend ultimately reports measurement results $\{s, c_s\}$ for measurement bitstrings $s \in \{0,1\}^m$ and cumulative counts c_s for m classical bits. The probability of measuring s is accordingly

$$p(s) = \frac{c_s}{\sum_{s' \in \{0,1\}^m} c_{s'}} \equiv \frac{c_s}{n_\mathrm{s}}. \tag{17}$$

Given the measurement counts, the expectation value $\langle \sigma_i^z \rangle$ can be calculated as

$$\langle \sigma_i^z \rangle = \langle \psi | \sigma_i^z | \psi \rangle = p_i(0) - p_i(1), \qquad p_i(b) = \frac{1}{n_\mathrm{s}} \sum_{\substack{s \in \{0,1\}^m \\ s_i = b}} c_s, \tag{18}$$

where $|\psi\rangle$ is the quantum state before measurement and $p_i(b)$ is the probability of qubit i yielding a measurement bit b. The notation s_j denotes digit j of the bitstring s. Through basis transformations implemented in the circuit, these computational-basis measurements can be used to recover different quantities of interest.

Supplementary Note 3. QUANTUM COMPUTING METHODS

A. Quantum Algorithms

In this section, we describe our implementation of the time-evolution of states and iterative quantum phase estimation on digital quantum computers. All experiments on quantum hardware are run through the IBM Q platform.

1. *Time Evolution*

The Schrödinger equation describes the time-evolution of quantum states under a Hamiltonian H,

$$\frac{\mathrm{d}\,|\psi(t)\rangle}{\mathrm{d}t} = -iH\,|\psi(t)\rangle\,, \tag{19}$$

where we have set $\hbar = 1$. Given an initial quantum state $|\psi_0\rangle$, the time-evolved state at time t is given by $|\psi(t)\rangle = e^{-iHt}\,|\psi_0\rangle$ for time-independent H. Note the propagator e^{-iHt} is unitary since H is Hermitian in our models, and

hence can be implemented on quantum circuits. This can be done through trotterization (Supplementary Note 3 B 2), which entails decomposing H in the spin-1/2 basis and performing a truncated expansion, or through a circuit recompilation procedure (Supplementary Note 3 B 3), which entails optimizing gate parameters on an circuit ansatz to approach the propagator. In this work, we have mostly employed circuit recompilation, which we optimize to handle the complexity of our Hamiltonians. The quantum circuit implementing time-evolution then consists of the initialization of $|\psi_0\rangle$, the e^{-iHt} block, and desired measurements—see Supplementary Figure 1a for a circuit diagram. The initialization of $|\psi_0\rangle$ is summarized in Supplementary Table 2.

Our interest is in accessing the occupancy expectation $\langle O_i\rangle = \langle c_i^\dagger c_i\rangle$ at each site of $|\psi(t)\rangle$, and the fidelity of $|\psi(t)\rangle$ relative to $|\psi_0\rangle$, to probe the time-evolution of states under H. The former reports on the spatial localization of states, and the latter reports on the speed of time-evolution away from $|\psi_0\rangle$. To measure $\langle O_i\rangle$ for sites $i \in \{1, 2, \ldots, n\}$, we perform computational basis measurements on all n simulation qubits, since $c_i^\dagger c_i = (1 - \sigma_i^z)/2$ from the Jordan-Wigner transform (see Supplementary Note 3 B 1). This applies regardless of the circuit generation technique used—trotterization or circuit recompilation—since we map single-qubit $|0\rangle$ to the unoccupied and $|1\rangle$ to the occupied fermionic states. We remind that $\sigma^z|0\rangle = |0\rangle$ and $\sigma^z|1\rangle = -|1\rangle$, therefore $\langle c_i^\dagger c_i\rangle = 0$ when qubit i is projectively measured in the $|0\rangle$ state and $\langle c_i^\dagger c_i\rangle = 1$ when in $|1\rangle$, as indeed expected. Suppose the measurement counts are c_s for measurement bitstring $s \in S = \{0, 1\}^n$, then it can be seen that

$$\langle O_i\rangle = \frac{1 - \langle\sigma_i^z\rangle}{2} = \sum_{\substack{s\in S\\ s_i=1}} c_s \Big/ \sum_{s\in S} c_s. \tag{20}$$

The set of measurements $\langle\sigma_i^z\rangle$ is cheap in circuit depth and enables access to $\langle O_i\rangle$ as desired; but does not report on the relative phase between the basis states $|s\rangle$, needed to compute the state fidelity $\mathcal{F}(\psi(t), \psi_0) = |\langle\psi_0|\psi(t)\rangle|^2$. Measuring $\mathcal{F}(\psi(t), \psi_0)$ is in general costly, and not entirely practical on current-generation quantum hardware. For example, without additional qubits, the fidelity between two state $U_1|0\rangle$ and $U_2|0\rangle$ can be recovered by measuring the probability of all-0 outputs on $U_2^\dagger U_1|0\rangle$; but the circuit involved is essentially double the depth of a single time-evolution propagator. To preserve shallow depth, quantum state tomography [33, 57–59] can instead be used on the two state separately, but this requires a number of circuits scaling exponentially with n. An alternative is the SWAP test [60, 61], requiring only a single circuit; but both states must be simultaneously prepared, necessitating at least $2n$ qubits in total. Furthermore, the long-range controlled-SWAP gates needed are expensive in circuit depth, when transpiled into nearest-neighbour 2-qubit gates suitable for hardware. Thus, instead of measuring $\mathcal{F}(\psi(t), \psi_0)$, we use an alternate fidelity measure $\mathcal{F}_O(\psi(t), \psi_0)$, termed the occupancy fidelity and defined as

$$\mathcal{F}_O(\psi_1, \psi_2) = \left|\mathbf{O}_1^\dagger \mathbf{O}_2\right|^2, \tag{21}$$

where $\mathbf{O}_1 = \begin{bmatrix}\langle O_1\rangle_1 & \langle O_2\rangle_1 & \ldots \langle O_n\rangle_1\end{bmatrix}^\intercal$ is the occupancy vector for $|\psi_1\rangle$ and likewise for $\mathbf{O}_2$. The form of the occupancy fidelity closely resembles that of the state fidelity; it serves the same purpose of reporting on the extent of evolution away from $|\psi_0\rangle$, based on occupancy expectations instead of the full quantum state. Since we readily measure $\langle O_i\rangle$, the occupancy fidelity $\mathcal{F}_O(\psi(t), \psi_0)$ can be accessed at no additional cost circuit-wise; that the occupancy vectors are $\mathcal{O}(n)$ large also means the calculation is classically efficient. Note error mitigation procedures (see Supplementary Note 3 C) are applied to the measurement counts c_s before recovering $\langle\sigma_i^z\rangle$ and $\mathcal{F}_O(\psi(t), \psi_0)$ in our experiments.

We note that the occupancy fidelity $\mathcal{F}_O(\psi_1, \psi_2)$ do not behave identically to the state fidelity $\mathcal{F}(\psi_1, \psi_2)$; but they are similar in most cases. In the extreme case, orthogonal states can have perfect occupancy fidelity; take for instance the product states $|+\rangle|1\rangle$ and $|-\rangle|1\rangle$. But the converse cannot occur, that is, two states cannot have zero occupancy fidelity but perfect state fidelity. Despite this distinction, the metric of occupancy fidelity suffices for our purposes, in the context of proving the difference in behaviour of topological and non-topological states.

2. *Iterative Quantum Phase Estimation*

Given $U|\psi\rangle = e^{2\pi i\phi}|\psi\rangle$ for a unitary U and an eigenstate $|\psi\rangle$, (traditional) quantum phase estimation (QPE) allows the measurement of eigenphase $\phi \in [0, 1)$, in principle to arbitrary precision [48, 62–64]. Note that the eigenvalues of a unitary have unity modulus, so there is no loss of generality. Setting $U = e^{-iHt}$ then allows the inference of eigenenergy $E = -2\pi\phi/t$ of $|\psi\rangle$ from the eigenphase, enabling the probing of the bandstructure of H. A standard circuit diagram for QPE is shown in Supplementary Figure 1d. Notably, each ancilla qubit measures a single bit of the binary representation of ϕ, hence to measure ϕ to reasonable ($< 5\%$) precision requires $\mathcal{O}(5)$ ancillae, in addition to the n simulation qubits. Furthermore, with the controlled-unitaries entangling each ancilla with the simulation

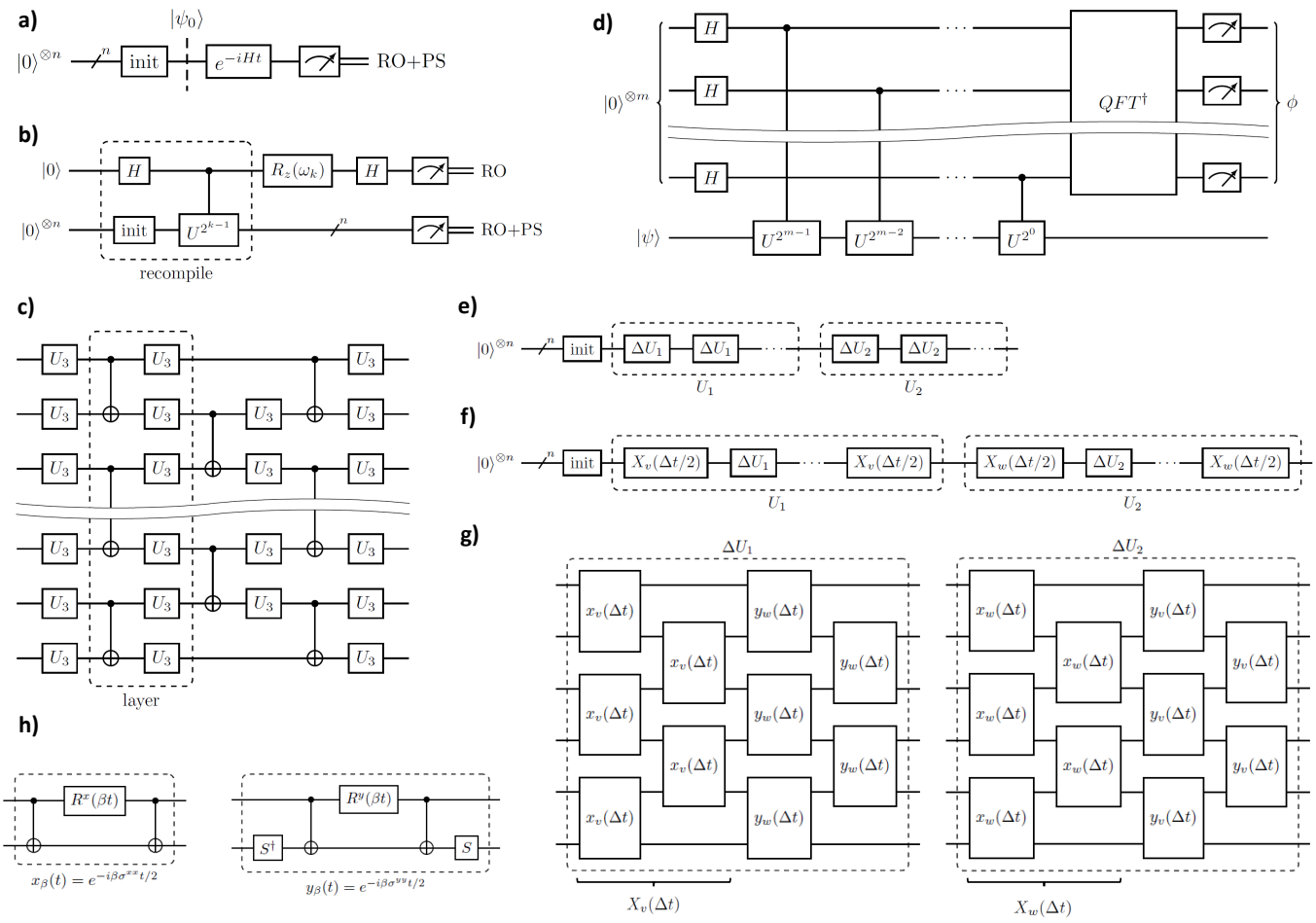

Supplementary Figure 1. **Summary of quantum circuits and circuit components.** **(a)** Time-evolution and **(b)** iterative quantum phase estimation (IQPE) circuit schematics. **(c)** Circuit ansatz for recompilation. **(d)** Circuit for traditional quantum phase estimation (QPE). The m ancilla qubits accommodates the reconstruction of the binary representation of the eigenphase ϕ. Circuit schematics for **(e)** first-order trotterization and **(f)** second-order symmetric trotterization of H^{SSH}, showing the concatenated U_1 and U_2 components (see Supplementary Note 3 B 2 for breakdown) and their constituent trotter steps; **(g)** structure of each trotter step, comprising even-odd parallelized $e^{-i\beta\sigma^{xx}t/2}$ and $e^{-i\beta\sigma^{yy}t/2}$ blocks; **(h)** implementation of aforementioned exponentiated Pauli strings.

qubits, and the inverse Fourier transform to shift from the Fourier basis into the computational basis for readout, means that QPE circuits are deep.

To reduce circuit breadth and depth, we use *iterative* quantum phase estimation (IQPE), which has only a single ancilla qubit and controlled-unitary block [65, 66]; the inverse Fourier transform for a single qubit is simply a Hadamard gate. Truncating the binary expansion of $\phi = 0.\phi_1\phi_2\ldots\phi_m$ to m bits, we iterate from $k = m$ to $k = 1$, measuring from the least to the most significant bit. In the circuit for the $k = m$ iteration, a controlled-$U^{2^{m-1}}$ block is applied, and the ancilla qubit is measured to determine ϕ_m. It can be shown that the probability p_0 of measuring an ancilla state of $|0\rangle$ is $\cos^2[(0.\phi_m)\pi]$ in the absence of noise, which is unity for $\phi_m = 0$ and zero for $\phi_m = 1$; of course, in the presence of noise measuring ϕ_m is no longer strictly deterministic, but the inference of $\phi_m = 0$ if $p_0 > 1/2$ and $\phi_m = 1$ otherwise can still be applied. Subsequently, in iteration k, a controlled-$U^{2^{k-1}}$ block is applied, and a feedback $R_z(\omega_k)$ rotation is applied to rotate off the phase due to the previous bits, before likewise inferring ϕ_k. The feedback angle is $\omega_k = -2\pi(0.0\phi_{k+1}\phi_{k+2}\ldots\phi_m)$. Clearly, to measure ϕ to m bits of precision, m iterations are needed. A circuit diagram of the IQPE circuit is given in Supplementary Figure 1b; we perform circuit recompilation (Supplementary Note 3 B 3) to implement the initialization of $|\psi\rangle$ and the controlled-unitary block. Note readout error mitigation (Supplementary Note 3 C 1) is applied to all qubits, and post-selection is applied to the simulation qubits to select a specific number sector (Supplementary Note 3 C 2).

There are several points to note. Firstly, it is not strictly necessary that the input state $|\psi\rangle$ be an eigenstate of U; an arbitrary $|\psi\rangle$ can always be written in the eigenbasis of U and superposition collapse during measurement will

produce an eigenphase ϕ associated with an eigenstate of U. In principle, repeating QPE with randomly generated $|\psi\rangle$ will eventually record all eigenphases ϕ and hence the bandstructure of H. However, in the presence of noise, it is beneficial to choose $|\psi\rangle$ with good overlap with an eigenstate of U, especially in IQPE—the issue is that near-equal overlaps with two or more eigenstates could result in $p_0 \approx 1/2$ in an iteration, and an incorrect inference would produce an erroneous ϕ. Secondly, the 2π periodicity of ϕ implies $2\pi\phi + 2\pi\ell = -Et$ for any $\ell \in \mathbb{Z}$, so the mapping $\phi \to E$ is multi-valued and one cannot infer a unique E from a single QPE instance. To infer E correctly one may choose a sufficiently small t to force $\ell = 0$, and to decide the sign of E one examines the slope between ϕ and t. To estimate the appropriate range of t, it is helpful to estimate the largest $|E|$ from the form of H.

To overcome these inherent limitations, we provide our IQPE instances with initial guesses $\{(|\psi\rangle, E)\}$ from exact diagonalization. This is classically tractable since we are interested in specific particle number sectors, in particular the 1-particle and 2-particle sectors, whose Hilbert spaces are not exponentially large with number of sites n. Indeed, the 1-particle and 2-particle subspaces are only of dimensionality $\mathcal{O}(n)$ and $\mathcal{O}(n^2)$; that is, the restricted Hamiltonian matrices are $\mathcal{O}(n \times n)$ and $\mathcal{O}(n^2 \times n^2)$ large. Since classical diagonalization is polynomially efficient in the size of the matrix, computing initial guesses $\{(|\psi\rangle, E)\}$ takes polynomial time and space. To be clear, the q-particle restricted Hamiltonian matrix $H^{[q]}$ is H with only rows and columns corresponding to q-particle basis states retained. In fact, the following construction can be found for the 1-particle sectors,

$$\left(H^{\mathrm{SSH}}\right)^{[1]} = \begin{bmatrix} E_0 & T_0 & & & & \\ T_0^\dagger & E_0 & T_0 & & & \\ & T_0^\dagger & E_0 & T_0 & & \\ & & \ddots & \ddots & \ddots & \\ & & & T_0^\dagger & E_0 & T_0 \\ & & & & T_0^\dagger & E_0 \end{bmatrix}, \qquad \left(H^{\mathrm{KC}}\right)^{[1]} = -\frac{1}{2}\begin{bmatrix} E_1 & T_1 & T_2 & & & \\ T_1^\dagger & E_1 & T_1 & T_2 & & \\ T_2^\dagger & T_1^\dagger & E_1 & T_1 & T_2 & \\ & \ddots & \ddots & \ddots & \ddots & \ddots \\ & & T_2^\dagger & T_1^\dagger & E_1 & T_1 \\ & & & T_2^\dagger & T_1^\dagger & E_1 \end{bmatrix}, \tag{22}$$

$$E_0 = \begin{bmatrix} 0 & v \\ v & 0 \end{bmatrix}, \qquad T_0 = \begin{bmatrix} 0 & 0 \\ w & 0 \end{bmatrix}, \qquad E_1 = 2\begin{bmatrix} \mu & 0 \\ 0 & \mu \end{bmatrix}, \qquad T_1 = \begin{bmatrix} v_1 & \Delta_1 \\ -\Delta_1 & -v_1 \end{bmatrix}, \qquad T_2 = \begin{bmatrix} v_2 & \Delta_2 e^{i\phi} \\ -\Delta_2 e^{-i\phi} & -v_2 \end{bmatrix},$$

with basis in descending binary order by convention, $\{|100\ldots\rangle, |010\ldots\rangle, \ldots, |\ldots 001\rangle\}$, and similar constructions can be given for the 2-particle sectors. Then, given eigenvector $[\alpha_1 \ \alpha_2 \ \ldots \ \alpha_N]^\intercal$ of $H^{[q]}$ with eigenenergy E, and supposing the corresponding basis states of $H^{[q]}$ are $\{|s_1\rangle, |s_2\rangle, \ldots, |s_N\rangle\}$ for fermionic occupancy bitstrings s_i, we may recover the $|\psi\rangle$ in the full Hilbert space of H as

$$|\psi\rangle = \sum_{i=1}^{N} \alpha_i \left[\prod_{j=1}^{n} \left(c_j^\dagger\right)^{s_{ij}}\right] |\mathrm{vac}\rangle .$$

Furthermore, we exploit additional optimizations to enhance computational efficiency. Firstly, as noted earlier, the input states $|\psi\rangle$ need not precisely be an eigenstate of U; this implies the diagonalization of $H^{[q]}$ need not be performed with full precision, and the diagonalization can be computed more quickly with relaxed error thresholds. In fact, it is not necessary to compute new initial guesses for every IQPE instance—prior guesses can be re-used, so long as they belong in a close-by neighborhood in parameter space. Also, in non-interacting cases, the 2-particle basis states are exactly the product of 1-particle states; then one needs only diagonalize $H^{[1]}$ to produce initial guesses for both sectors.

B. Circuit Generation

Time-evolution and IQPE circuits require the implementation of the $U(t) = e^{-iHt}$ propagator. While topological Hamiltonians associated with winding number invariants are most conveniently written in fermionic second-quantized forms, qubits are inherently two-state systems. To represent our topological Hamiltonians and perform time-evolution, there is a need to convert between the fermionic to the spin-1/2 Pauli basis.

1. *Jordan-Wigner transformation*

For pedagogical purposes, we first present the well-known Jordan-Wigner (JW) transformation that has traditionally been used for mapping between fermions and spin-1/2s [45–48]; note that in this work, most of our quantum circuits

are generated via the more sophisticated circuit recompilation technique described later (Supplementary Note 3 B 3). One writes

$$c_j^\dagger = \left(\prod_{k=1}^{j-1} \sigma_k^z\right) \sigma_j^-, \qquad c_j = \left(\prod_{k=1}^{j-1} \sigma_k^z\right) \sigma_j^+, \tag{23}$$

where $\sigma_j^\pm = \left(\sigma_j^x \pm i\sigma_j^y\right)/2$ are the Pauli raising and lowering operators, and number operator $n_k = c_k^\dagger c_k = (1-\sigma_k^z)/2$. To avoid confusion, note this Pauli basis is different from that used in representing the 2-component lattices in Supplementary Note 1. The occupancy-dependent phase factors in front of $c_j^\dagger$ and c_j, called strings, are necessary to enforce the fermionic anti-commutation relations. Indeed, one can check that this transformation preserves $\{c_j, c_k^\dagger\} = \delta_{jk}$ and $\{c_j^\dagger, c_k^\dagger\} = \{c_j, c_k\} = 0$ for all site pairs (j,k). By applying the above transform, one can decompose any fermionic quadratic tight-binding Hamiltonian in the Pauli (spin-1/2) basis,

$$H = \sum_{i,j=1}^{n} t_{ij} c_i^\dagger c_j + \text{h.c.} = \sum_{\boldsymbol{\mu}} \alpha_{\boldsymbol{\mu}} \sigma^{\boldsymbol{\mu}}, \qquad \sigma_j^{\boldsymbol{\mu}} = \prod_{k=1}^{|\boldsymbol{\mu}|} \sigma_{j+k-1}^{\boldsymbol{\mu}_k}, \tag{24}$$

where $\sigma^{\boldsymbol{\mu}}$ are products of Pauli matrices with $\boldsymbol{\mu}_j \in \{x,y,z\}$, and $t_{ij} \in \mathbb{C}$ and $\alpha_{\boldsymbol{\mu}} \in \mathbb{C}$ are coefficients. As explicit examples, we have

$$\begin{aligned}
H^{\text{SSH}} &= \underbrace{\frac{v}{2}\sum_{j=1}^{N} \sigma_{2j-1}^{xx}}_{X_v} + \underbrace{\frac{v}{2}\sum_{j=1}^{N} \sigma_{2j-1}^{yy}}_{Y_v} + \underbrace{\frac{w}{2}\sum_{j=1}^{N-1} \sigma_{2j}^{xx}}_{X_w} + \underbrace{\frac{w}{2}\sum_{j=1}^{N-1} \sigma_{2j}^{yy}}_{Y_w}, \\
H^{\text{KC}} &= \frac{\mu}{2}\sum_{j=1}^{N} \left(\sigma_{2j}^z - \sigma_{2j-1}^z\right) + \frac{v_1}{4}\sum_{j=1}^{N-1} \left(\sigma_{2j-1}^{xzx} + \sigma_{2j-1}^{yzy} - \sigma_{2j}^{xzx} - \sigma_{2j}^{yzy}\right) \\
&\quad + \frac{v_2}{4}\sum_{j=1}^{N-2} \left(\sigma_{2j-1}^{xzzzx} + \sigma_{2j-1}^{yzzzy} - \sigma_{2j}^{xzzzx} - \sigma_{2j}^{yzzzy}\right) \\
&\quad + \frac{\Delta_1}{2}\sum_{j=1}^{N-1} \left(\sigma_{2j}^{xx} + \sigma_{2j}^{yy} - \sigma_{2j-1}^{xzzx} - \sigma_{2j}^{yzzy}\right) + \frac{\Delta_2 e^{i\phi}}{4}\sum_{j=1}^{N-2} \left(\sigma_{2j}^{xzzx} + \sigma_{2j}^{yzzy} - \sigma_{2j-1}^{xzzzzx} - \sigma_{2j}^{yzzzzy}\right)
\end{aligned} \tag{25}$$

where we have labelled the terms in H^{SSH} by $X_{v,w}$ and $Y_{v,w}$ for convenience in the following subsection.

We remark that the JW-transform is not the only choice for mapping between the fermionic and spin-1/2 bases. It is a characteristic that the JW-transform stores fermionic occupancy information locally, but delocalizes parity information across all previous qubits—this manifests in the string phase factors. The parity map is opposite, storing parity locally but delocalizing occupancy across all previous qubits; and the Bravyi-Kitaev (BK) transformation [67] is a middle ground, delocalizing both parity and occupancy information, but with logarithmic scaling. In principle it is less costly circuit-wise to implement fermionic operators on a quantum computer using the BK scheme, but expected benefits at $\mathcal{O}(10)$ qubits for our purposes are negligible, and there is incurred complexity with applying the necessary update operations. Hence the JW-transform can often be the preferred choice, by virtue of its simplicity.

2. *Trotterization*

Decomposing the Hamiltonian in the Pauli basis does not lead immediately to a circuit implementation of the $U(t) = e^{-iHt}$ propagator; the problem is that the Pauli strings summed over may not commute. It is known that $e^{A+B} \neq e^A e^B$ when $[A,B] \neq 0$ for operators A and B, hence one cannot simply implement the exponentiated Pauli strings one-by-one and glue the circuits together. This problem is addressable with the Suzuki-Trotter (ST) decomposition [35, 43, 68–71]. The main observation is that

$$e^{A+B} = \lim_{n\to\infty} \left(e^{A/n} e^{B/n}\right)^n, \tag{26}$$

hence we break $e^{-iHt} = \left(e^{-iH\Delta t}\right)^M$ for $\Delta t = t/M$ into $M \gg 1$ pieces, called trotter steps, each of which can be expanded to small error. For $H = \sum_{\boldsymbol{\mu}} \alpha_{\boldsymbol{\mu}} \sigma^{\boldsymbol{\mu}}$, we have the first-order trotterization

$$e^{-iH\Delta t} = \left(\prod_{\boldsymbol{\mu}} e^{-i\alpha_{\boldsymbol{\mu}}\sigma^{\boldsymbol{\mu}}\Delta t}\right) + \mathcal{O}\left(\frac{1}{M^2}\right), \tag{27}$$

and hence the total error incurred over M steps is $\mathcal{O}(1/M)$, suppressible by increasing M. Each of the $e^{-i\alpha_\mu \sigma^\mu \Delta t}$ terms can be straightforwardly implemented on a quantum circuit, since $\sigma^{\boldsymbol{\mu}}$ is a Pauli string. There are higher-order ST decompositions as well [35, 72]. Splitting $H = \sum_{\boldsymbol{\mu}} \alpha_{\boldsymbol{\mu}} \sigma^{\boldsymbol{\mu}} + \sum_{\boldsymbol{\nu}} \alpha_{\boldsymbol{\nu}} \sigma^{\boldsymbol{\nu}}$, the second-order symmetric trotterization can be written as

$$e^{-iH\Delta t} = \left(\prod_{\boldsymbol{\mu}} e^{-i\alpha_\mu \sigma^\mu \Delta t/2}\right)\left(\prod_{\boldsymbol{\nu}} e^{-i\alpha_\nu \sigma^\nu \Delta t}\right)\left(\prod_{\boldsymbol{\mu}} e^{-i\alpha_\mu \sigma^\mu \Delta t/2}\right) + \mathcal{O}\left(\frac{1}{M^3}\right), \tag{28}$$

hence yielding total error $\mathcal{O}\left(1/M^3\right)$. The symmetry of the decomposition allows gate layers to be combined between adjacent trotter steps, reducing circuit depth.

We illustrate and compare the first- and second-order trotterized circuits for the SSH model in Supplementary Figure 1e–h. Gates acting on different qubits are parallelized whenever possible to reduce circuit depth; this is most efficiently done by splitting the sums into odd and even terms. For the second-order symmetric trotterization, we note $[X_v, X_w] = [Y_v, Y_w] = 0$ and $[X_v, Y_v] = [X_w, Y_w] = 0$, and so H^{SSH} splits into two commuting groups $X_v + Y_w$ and $X_w + Y_v$. Accordingly, we may write the propagator $U(t) = e^{-iHt} = U_2(t)U_1(t)$, for $U_1(t) = e^{-i(X_v+Y_w)t}$ and $U_2(t) = e^{-i(X_w+Y_v)t}$, yielding the trotterization structure shown. Notice that the implementation of $e^{-i\beta\sigma^{xx}t/2}$ and $e^{-i\beta\sigma^{yy}t/2}$ unitaries require 2 CX layers each; in general the necessary CX depth increases with the weight of the Pauli string.

3. *Circuit Recompilation*

Traditional trotterization results in deep circuits for all but the simplest Hamiltonians—consider that the time-evolution unitaries $U_{\mathrm{SSH}}(t)$ and $U_{\mathrm{KC}}(t)$ require 4 and > 16 CX layers per trotter step. Ballpark estimates of $T_1 \approx T_2 \approx 60\,\mu\mathrm{s}$ and CX gate time of 440 ns suggest a maximum feasible circuit depth of ∼140 CX layers; in practice hardware results degrade after ∼20 CX layers, without accounting for the presence of other gates in the circuit. It is advantageous to identify more compact circuits serving in the same capacity. This motivates the circuit recompilation procedure [43, 73–75] discussed here, which we employ for our computations on IBM Q hardware.

We adopt a circuit ansatz comprising an initial layer of U_3 gates on all qubits followed by n_{L} ansatz layers, each comprising a layer of CX gates entangling adjacent qubits and a layer of U_3 single-qubit rotations (see Supplementary Figure 1c). This ansatz provides sufficient freedom for the unitaries in this work at modest $n_{\mathrm{L}} \leq 8$ circuit depth. Each U_3 gate in the ansatz is associated with angles (θ, ϕ, λ); we collate all of them into parameter vector $\boldsymbol{\theta}$. Then, given a target circuit unitary V and an initial state $|\psi_0\rangle$, we numerically treat the optimization problem

$$\underset{\boldsymbol{\theta}}{\mathrm{argmax}}\, F(V_{\boldsymbol{\theta}} |\psi_0\rangle, V |\psi_0\rangle) = \underset{\boldsymbol{\theta}}{\mathrm{argmax}} \left| \langle\psi_0| V_{\boldsymbol{\theta}}^\dagger V |\psi_0\rangle \right|^2, \tag{29}$$

where $V_{\boldsymbol{\theta}}$ is the circuit ansatz unitary with parameters $\boldsymbol{\theta}$. Then the recompiled circuit is the ansatz with optimal parameters $\boldsymbol{\theta}^*$ fixing the U_3 gates. In our implementation, we use a tensor network-based noiseless circuit simulator [76] to compute $V_{\boldsymbol{\theta}}$ and the limited-memory Broyden–Fletcher–Goldfarb–Shanno algorithm with box constraints (L-BFGS-B) to perform the optimization [77, 78], with basin hopping for 10^2 hops and at most 10^3 iterations per hop. The optimization is terminated at target fidelity $F \geq 99.99\%$. This procedure produces recompiled circuits typically in seconds to minutes; to further aid efficiency we store all recompiled circuits in a persistent cache for reuse. Note the recompilation procedure works for arbitrary circuit unitary V—so long as n_{L} provides sufficient freedom for fitting.

As mentioned in the main text, with larger fermion numbers, the increased entanglement in the time-evolved states makes the optimization of gate parameters more difficult, and a larger number of iterations must typically be run, thus impairing recompilation speed. To mitigate this, we modify the optimizational problem to focus only on the relevant sectors. Specifically, since our Hamiltonians are all number-conserving, we need only maximize fidelity in the k-particle sector for a k-particle initial state; fidelity in other sectors are inconsequential, as results falling in them violate symmetry and are discarded by post-selection (see Supplementary Note 3 C 2). This enables improved recompilation performance for multi-fermion states.

We provide a comparison of the performance of circuit recompilation against first- and second-order trotterization in Supplementary Figure 2a, on the H^{SSH} model. The difference in circuit depth is drastic—circuit recompilation yields comparable error but with an order of magnitude fewer CX layers. As noted, the CX cost of trotterization arises from the implementation of $e^{-i\sigma^{\boldsymbol{\mu}}t/2}$ terms in each trotter step; the trotterized circuit depth for H^{KC} will be significantly worse than H^{SSH}, due to the larger number and greater weight of the Pauli strings in the Hamiltonian. The motivation to utilize circuit recompilation is therefore abundantly clear; in fact, acquiring quantum simulation results of the same quality as that reported here is essentially infeasible, on current-generation hardware, with traditional trotterization.

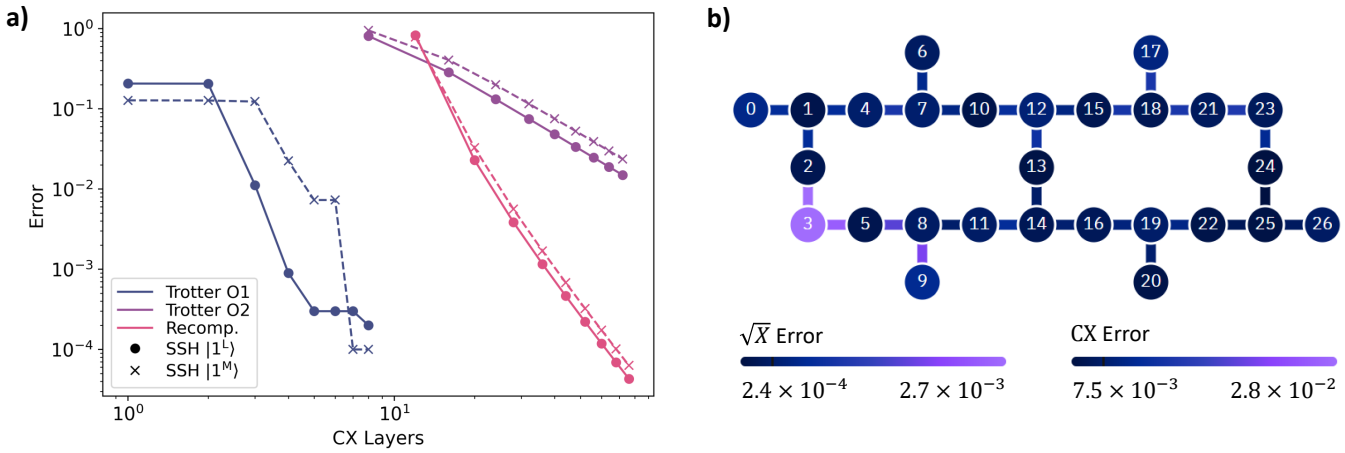

Supplementary Figure 2. **Comparison of circuit implementation error and example of qubit layout on IBM Q device. (a)** Comparison of circuit implementation error $\mathcal{E} = 1 - \mathcal{F}(\psi^*(t), \psi(t)) = 1 - |\langle\psi^*(t)|\psi(t)\rangle|^2$, where $\psi^*(t) = e^{-iHt}\psi_0$ is the exact time-evolved statevector and $\psi(t)$ is that yielded by the circuit, using first- (O1) and second-order (O2) trotterization, and circuit recompilation. The H^{SSH} model in the topological phase ($\nu = 1$; $w/v = 2$) is used, with initial states $|1^{\mathrm{L}}\rangle$ and $|1^{\mathrm{M}}\rangle$; evolution time is fixed at $t = 1$. For trotterization, the number of trotter steps (M) is varied; for circuit recompilation, the number of ansatz layers (n_{L}) is varied. Evidently, circuit recompilation yields far lower errors than either first or second-order trotterization, for comparable number of CX layers. **(b)** Illustration of qubit layout for *ibmq_paris*, with typical $\sqrt{X}$ and CX gate error rates, as reported from the IBM Q daily calibration; color shading on qubits and qubit connections reflect gate errors in correspondence to the color chart. Layout visualization and calibration data were obtained from the IBM Quantum portal [79].

C. Error Mitigation

1. *Readout Error Mitigation (RO)*

Measurements on current-generation quantum hardware are imperfect—there is a chance of measuring $|1\rangle$ when a qubit is in the $|0\rangle$ state, and vice versa. A method to correct these errors is to record the measurement bit-flip probabilities on each qubit by running calibration circuits beforehand; then given raw measurement counts from experiments, the inverse problem is solved to estimate the true measurement counts [33, 35–38]. We first discuss *complete* readout mitigation. Consider a quantum circuit terminating with measurements on all n qubits. Then the state of the qubits before measurement lives in Hilbert space $\mathcal{H}$ with basis states $\{|s\rangle : s \in \{0,1\}^n\}$, that is, s enumerates all binary strings of length n. Furthermore, suppose we have a calibration matrix M with entry[1] M_{ij} recording the probability of measuring bitstring $i \in \{0,1\}^n$ when the true result is $j \in \{0,1\}^n$. Denoting the raw measurement count c_s for bitstring $s \in \{0,1\}^n$, the relation between the corrected counts c'_s and c_s is

$$c_s = \sum_{r\in\{0,1\}^n} M_{sr} c'_r. \tag{30}$$

Equivalently, collating the measurement counts into $\mathbf{c} = [c_0 \;\; c_1 \;\; \ldots \;\; c_{2^n-1}]^\intercal$ and $\mathbf{c}' = [c'_0 \;\; c'_1 \;\; \ldots \;\; c'_{2^n-1}]^\intercal$, we have the linear maps $M\mathbf{c}' = \mathbf{c} \iff \mathbf{c}' = M^+\mathbf{c}$ where M^+ is the pseudoinverse of M. The estimated $\mathbf{c}'$ may carry negative entries due to the approximate M and numerical errors; we zero these entries as they are unphysical. Note *Qiskit* [33, 34] provides a procedure of least-squares fitting to estimate $\mathbf{c}'$ from $\mathbf{c}$, but we found the computational cost too large to be feasibly used for more than a handful of qubits—hence the choice of direct pseudoinverse computation.

The matrix M can be constructed by running calibration circuits [33, 34]. In circuit $\mathcal{C}_j$ we prepare $|j\rangle$ and measure all qubits; the resulting measurement probability of i then sets M_{ij}, that is, $M_{ij} = c_i / \sum_i c_i$ from $\mathcal{C}_j$. Accordingly, complete readout mitigation requires 2^n calibration circuits to be run. The advantage is that correlations in measurement errors on different qubits—more precisely qubit states—are recorded; but the number of calibration circuits

[1] Binary bitstrings are converted to their base-10 representations when acting as integer indices. This convention is followed throughout this article for notational simplicity.

poses feasibility limitations. In our implementation, the required calibration circuits are prepended to each IBM Q experiment to be run. The machines available (*ibmq_manhattan*, *ibmq_paris*, *ibmq_toronto* and *ibmq_boeblingen*) limit at most 900 circuits per job, thereby constraining $n \leq 9$ for complete readout mitigation to be usable. One may calibrate M and reuse the same matrix for a period of time, so long as the same qubits are used in circuits; but the noise characteristics on hardware drift over time, and performing the calibration on-demand immediately before each experiment yields better results.

The circuit breadth limitation motivates *tensored* readout mitigation. Let us split $\mathcal{H} = \mathcal{H}_1 \otimes \mathcal{H}_2$, with basis states $\{|s_1\rangle |s_2\rangle = |s_1 s_2\rangle : s_1 \in \{0,1\}^{n_1}, s_2 \in \{0,1\}^{n_2}\}$. That is, we regard the quantum register of $n = n_1 + n_2$ qubits as split into two, containing n_1 and n_2 qubits respectively. Then supposing we have calibration matrices $M^{(1)}$ and $M^{(2)}$ for the two registers, we may construct $M = M^{(1)} \otimes M^{(2)}$, and $\mathbf{c}' = M^{+}\mathbf{c}$ then likewise applies. In practice, it is preferable to avoid the explicit computation of $M^{(1)} \otimes M^{(2)}$ since the matrices are exponentially large; instead we write

$$c_{s_1 s_2} = \sum_{r_1 \in \{0,1\}^{n_1}} \sum_{r_2 \in \{0,1\}^{n_2}} M_{s_1 r_1} M_{s_2 r_2} c'_{r_1 r_2}, \tag{31}$$

and likewise compute $\mathbf{c}'$ using the pseudoinverses of $M^{(1)}$ and $M^{(2)}$. Note we require at most $2^{n_1} + 2^{n_2} < 2^n$ calibration circuits to obtain $M^{(1)}$ and $M^{(2)}$—in practice fewer, since each circuit calibrating the first register can be merged with one calibrating the other—but this is at the expense of neglecting correlations in measurement errors between qubits belonging to different registers. In our implementation, we choose $n_1 = \lceil n/2 \rceil$ and $n_2 = n - n_1$, enabling feasible readout mitigation for $n \geq 13$ as needed in our experiments; for example $n = 12$ qubits requires only 96 calibration circuits. We utilize tensored readout mitigation for all circuits containing $n \geq 10$ qubits; otherwise complete readout mitigation is used. The effect of readout mitigation on hardware data quality is smaller than that of post-selection, but it nonetheless remains an important error mitigation step; the effectiveness of post-selection diminishes when readout mitigation is not first performed.

2. *Post-Selection (PS)*

Readout error mitigation reduces the effect of measurement errors, but does not mitigate errors incurred during the execution of gate rounds in the circuit. We use a post-selection procedure [35, 80] to mitigate these errors to a limited extent. Suppose the Hamiltonian H has symmetry (observable) $\mathcal{S}$ such that $[H, \mathcal{S}] = 0$; then $\langle \mathcal{S} \rangle$ is a conserved quantity. It must therefore be that $\langle \psi(t)|\mathcal{S}|\psi(t)\rangle = \langle \psi(0)|\mathcal{S}|\psi(0)\rangle$ for a time-evolved state $|\psi(t)\rangle = e^{-iHt}|\psi(0)\rangle$ and initial state $|\psi(0)\rangle$. Suppose furthermore that $\langle \mathcal{S} \rangle_t = \langle \psi(t)|\mathcal{S}|\psi(t)\rangle$ can be conveniently measured on the quantum circuits and $\langle \mathcal{S} \rangle_0$ is known; then if we find $\langle \mathcal{S} \rangle_t \neq \langle \mathcal{S} \rangle_0$, we may discard the measurement result as it is unphysical.

The Hamiltonians studied in this article conserve particle number, in that $[H, O] = 0$ for total particle number operator $O = \sum_{i=1}^{n} c_i^\dagger c_i$ over n sites. We take $\mathcal{S} = O$ for post-selection. Recall we may access site-wise occupancy expectation through computational-basis measurements on all simulation qubits (Supplementary Note 3 A 1); we piggy-back on these measurements for post-selection. This leads to the following post-selection rule—suppose the raw experiment counts are c_s for measurement bitstring $s \in \{0,1\}^n$, and that the initial state $|\psi(0)\rangle$ gives known $\langle O \rangle_0 \in \mathbb{N}$. Then the mitigated counts are $c'_s = c_s$ if $\sum_i s_i = \langle O \rangle_0$ for bits $s_i \in s$, and $c'_s = 0$ otherwise. That is, we discard measurement bitstrings that have the incorrect particle number as required by symmetry.

3. *Qubit Chain Selection*

The available quantum hardware provide more qubits than needed for our experiments—*ibmq_manhattan* comprises 65 qubits for instance—and there are significant variations in the quality of qubits within the same machine. It is therefore advantageous to select qubits of the highest quality to use for experiments on an on-demand basis. Note our circuit ansatz for compilation (see Supplementary Note 3 B 3) requires CX connections between all adjacent pairs of qubits but not longer-range connections; hence we seek qubit chains. Given the available non-faulty qubits and CX couplings between qubits, we construct a graph representation and perform breadth-first search to identify all distinct qubit chains of the required length n. Then we compute the following fitness function for each chain,

$$Q = 1 - \left\{ \prod_{i=1}^{n} \left(1 - E_i^{U_3}\right)^{n_\mathrm{L}+1} \left[\left(1 - E_{i,i-1}^{\mathrm{CX}}\right)\left(1 - E_{i,i+1}^{\mathrm{CX}}\right)\right]^{n_\mathrm{L}/2} \left(1 - E_i^{\mathrm{M}}\right) \right\}^{1/n}, \tag{32}$$

where $E_i^{U_3}$ is the calibrated U_3 gate error and E_i^{M} is the calibrated measurement error for qubit i, and $E_{i,j}^{\mathrm{CX}}$ is the calibrated CX gate error between qubits i and j. As before, n_L is the number of layers in the circuit recompilation

ansatz. The fitness Q is intended to emulate the structure of the recompilation circuit ansatz; we set $n_{\mathrm{L}} = 5$ as a typical value, and $E^{\mathrm{CX}}_{1,0} = E^{\mathrm{CX}}_{n,n+1} = 0$ by convention. We then pick the qubit chains with highest Q for experiments. Note the error rates are pulled from the daily calibration of IBM Q machines, and are hence only approximate in nature.

4. Repetitions & Averaging

To minimize the effects of stochastic noise, we run each circuit for the maximum allowable number of shots $n_{\mathrm{s}} = 8192$ in all our experiments. Furthermore, we perform repetitions $6 \leq n_{\mathrm{r}} \leq 20$ of each circuit, such that each submitted job to the IBM Q backends saturates the 900 circuits limit whenever possible. The effective number of shots is hence $n_{\mathrm{s}} n_{\mathrm{r}} \gtrsim 5 \times 10^4$ for each circuit. The degrading effects of stochastic noise on our results are further reduced by collating error-mitigated measurement bitstring counts over multiple qubit chains per machine, and multiple IBM Q machines; fluctuations in data due to noise are then averaged out. Note the performance of the machines exhibit a degree of variability—the error rates reported from the daily calibration may be inaccurate, qubits and CX connections between qubits can become faulty, and noise may cause sporadic degradation in quality of results. To filter these erroneous outliers out, we discard time series data that exhibit major discontinuities, which are unphysical; occupancy expectations must be continuous in time.

SSH Model

$\|\psi_0\rangle$	Initialization Circuit
$\|1^{\mathrm{L}}\rangle$	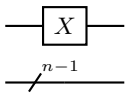
$\|1^{\mathrm{R}}\rangle$	Mirror $\|1^{\mathrm{L}}\rangle$
$\|1^{\mathrm{M}}\rangle$	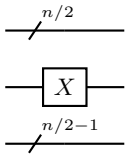
$\|2^{\mathrm{L}}_{11}\rangle$	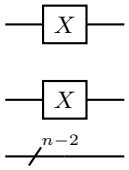
$\|2^{\mathrm{R}}_{11}\rangle$	Mirror $\|2^{\mathrm{L}}_{11}\rangle$
$\|2^{\mathrm{L}}_{101}\rangle$	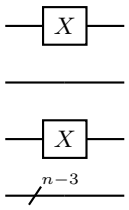
$\|2^{\mathrm{R}}_{101}\rangle$	Mirror $\|2^{\mathrm{L}}_{101}\rangle$
$\|2^{\mathrm{M}}\rangle$	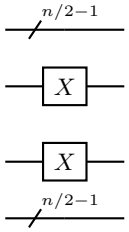
$\|2^{\mathrm{LR}}\rangle$	Concatenate $\|1^{\mathrm{L}}\rangle$ and $\|1^{\mathrm{R}}\rangle$

KC Model (BDI Class)

$\|\psi_0\rangle$	Initialization Circuit
$\|1^{\mathrm{L}}_j\rangle$ for $j \in \{1,2\}$	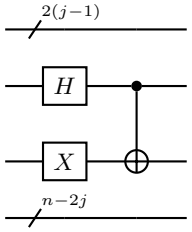
$\|1^{\mathrm{R}}_j\rangle$ for $j \in \{1,2\}$	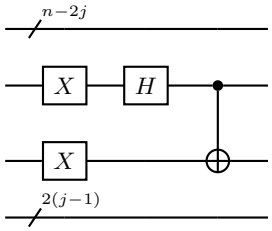
$\|1^{\mathrm{M}}\rangle$	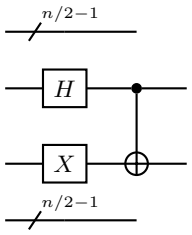
$\|2^{\mathrm{L}}\rangle$	Concatenate $\|1^{\mathrm{L}}_1\rangle$ and $\|1^{\mathrm{L}}_2\rangle$
$\|2^{\mathrm{R}}\rangle$	Concatenate $\|1^{\mathrm{R}}_1\rangle$ and $\|1^{\mathrm{R}}_2\rangle$
$\|2^{\mathrm{LR}}_{jk}\rangle$ for $j,k \in \{1,2\}$	Concatenate $\|1^{\mathrm{L}}_j\rangle$ and $\|1^{\mathrm{R}}_k\rangle$
$\|2^{\mathrm{M}}\rangle$	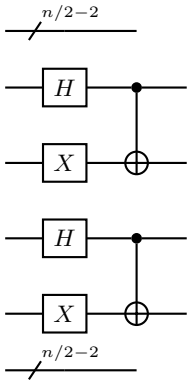

Supplementary Table 2. Initialization circuit components for the SSH and the BDI-class KC models, corresponding to the initialization blocks drawn in the diagrams of Supplementary Figure 1. Initial states for the D-class KC model are more complicated, and are absorbed into the circuit recompilation ansatz to minimize circuit depth.

Supplementary Note 4. ADDITIONAL RESULTS

Here we present several sets of additional results, complementing those given in the main paper. We recap the connection between the extended Kitaev model examined in our work and the more familiar Kitaev chain with only next-nearest (NN) neighbour hoppings and pairings, and provide time-evolution and IQPE observations on hardware. In the second subsection, we provide a more extensive set of results for the interacting H^{KC} with up to 4 fermions.

A. Su-Schrieffer-Heeger Model

The stability of $|1^{\mathrm{L}}\rangle$ is preserved even when mixed with non-SPT states localized on the neighbouring and next-neighbouring sites (Supplementary Figure 3a). We also show the 2-particle band structure of H^{SSH} obtained through IQPE (Supplementary Figure 3b); the topological phase is characterized by pairs of bands merging into degeneracy as $w/v \to \infty$, even though the zero energy midgap states can now correspond to either $\left|2^{\mathrm{LR}}\right\rangle$ or the product state of two particles with equal and opposite eigenenergies.

B. Simple Kitaev Chain

By removing the NNN hopping and pairing terms in H^{KC}, that is, by setting $v_2 = \Delta_2 = 0$, we can reduce the extended Kitaev model into the usual Kitaev chain with only NN hopping and pairing,

$$H^{\mathrm{KC}} = \mu \sum_{j=1}^{N} \left(c_j^\dagger c_j - d_i^\dagger d_j \right) + \frac{v_1}{2} \sum_{j=1}^{N-1} \left(c_j^\dagger c_{j+1} - d_i^\dagger d_{j+1} + \mathrm{h.c.} \right) + \frac{\Delta_1}{2} \sum_{j=1}^{N-1} \left(d_j^\dagger c_{j+1} - c_j^\dagger d_{j+1} + \mathrm{h.c.} \right), \tag{33}$$

which we call the simple Kitaev chain (SKC). The relation between the extended Kitaev model, SKC, and the SSH model had been previously introduced. The removal of NNN terms from the model restricts SKC to possess only the $\nu = 1$ topological and $\nu = 0$ trivial phase, analogous to the BDI-class extended Kitaev model but with the $\nu = 2$ phase no longer present. This means SKC has at most two topological zero modes, and like the SSH model, can support only a single boundary-localized fermion on each edge. We show this in Supplementary Figure 4a–b. The contrast in the persistence of boundary-localized states, relative to non-topological middle-localized states, is clear. We also present the 1-particle bandstructure of the SKC model in Supplementary Figure 4c, showing the transition between topological and trivial phases. The deviation of the breaking of zero mode degeneracy from the $\mu = v$ theoretical boundary is due to finite system size; as $N \to \infty$ (practically $N \gtrsim 20$ is sufficient) the deviation diminishes.

C. D-Class Extended Kiteav Chain with Added Interactions

In the main text, it was mentioned that the U_2 interaction has a similar but weaker effect as the U_3 interaction in stabilizing the non-topological 3- and 4-fermion states, that carry a greater number of fermions on an edge than the number of available topological modes. We present the complete set of hardware results in Supplementary Figure 5a–c, including occupancy density plots.

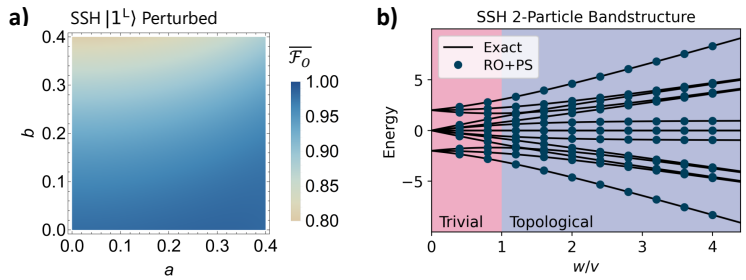

Supplementary Figure 3. **Additional results of non-interacting SSH model. (a)** Average occupancy fidelity $\overline{\mathcal{F}_O}$ of the superposed state $\sqrt{1-a^2-b^2}\,|1^{\mathrm{L}}\rangle + a\,|1^{\mathrm{L}}_{\mathrm{B}}\rangle + b\,|1^{\mathrm{L}}_{0\mathrm{A}}\rangle$ over time $t \in [0, 1.2]$, where $\left|1^{\mathrm{L}}_{\mathrm{B}}\right\rangle$ and $\left|1^{\mathrm{L}}_{0\mathrm{A}}\right\rangle$ are localized on neighbouring and next-neighbouring sites. The topologically-protected $|1^{\mathrm{L}}\rangle$ remains stable even amidst considerable perturbations. **(b)** 2-fermion band structure of H^{SSH} as accessed through IQPE. Results are on $n = 7$ qubits, one of which is an ancilla. IBM Q machines *ibmq_ toronto* and *ibmq_ guadalupe* were used.

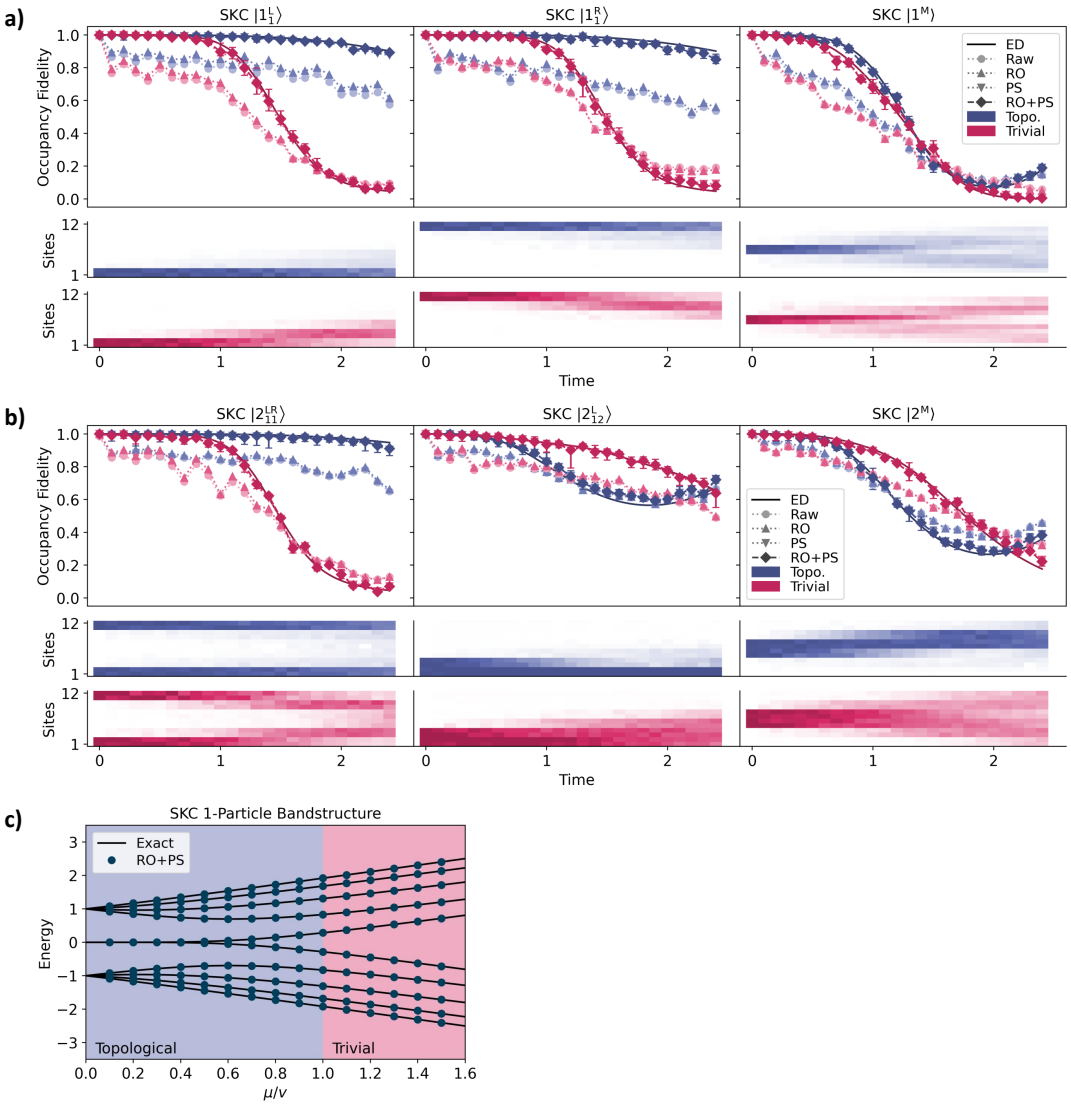

Supplementary Figure 4. **Additional results of non-interacting simple Kitaev chain.** Time-evolution results for various **(a)** 1-particle and **(b)** 2-particle states in the simple Kitaev chain (SKC) model. The $\nu = 1$ topological phase can support up to a single stable fermion localized on each edge, such as in $\left|1_1^{\mathrm{L}}\right\rangle$ and $\left|1_1^{\mathrm{R}}\right\rangle$. States that carry a larger number of boundary-localized fermions than available topological modes, such as $\left|2_{12}^{\mathrm{L}}\right\rangle$, are unstable. **(c)** Bandstructure of the 1-particle SKC model reconstructed through IQPE. All time-evolution results are computed on chains with $N = 6$ unit cells ($n = 12$ qubits), with error bars representing the min/max from repeated experiments across different qubit chains and machines (*ibmq_paris*, *ibmq_toronto*, *ibmq_manhattan*, and *ibmq_boeblingen*); IQPE results are for $n = 10$ chains with an additional ancilla qubit. Model parameter values are $\mu = 1/5$, $v = 1$ and $\Delta = 3/5$ for the topological phase, and $\mu = 5/4$, $v = 1$ and $\Delta = 1/2$ for the trivial phase, where applicable.

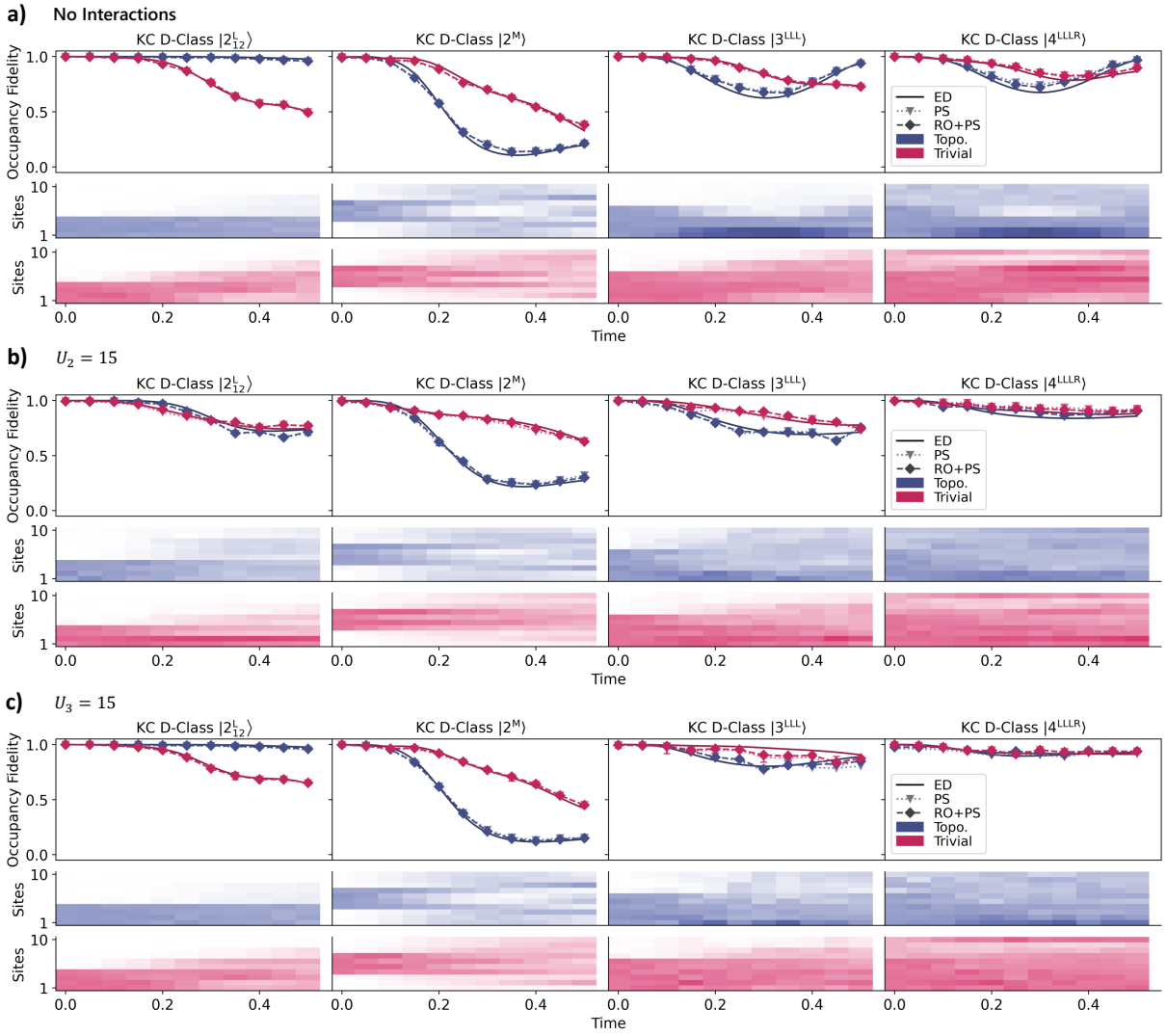

Supplementary Figure 5. **Additional results of interacting D-class extended Kitaev chain.** Time-evolution results without interactions **(a)**, and with added U_2 **(b)** and U_3 **(c)** interactions. As discussed, the U_2 and U_3 interactions have qualitatively similar stabilizing effects on the 3- and 4-fermion states. These results are computed on chains with $N = 5$ unit cells ($n = 10$ qubits), with error bars representing the min/max from repeated experiments across different qubit chains and machines (*ibmq_paris*, *ibmq_toronto*, *ibmq_manhattan*, and *ibmq_guadalupe*).

[1] Senthil, T. Symmetry-protected topological phases of quantum matter. *Annu. Rev. Condens. Matter Phys.* **6**, 299–324 (2015).

[2] Chiu, C.-K., Teo, J. C. Y., Schnyder, A. P. & Ryu, S. Classification of topological quantum matter with symmetries. *Rev. Mod. Phys.* **88**, 035005 (2016).

[3] Haldane, F. D. M. Nobel lecture: Topological quantum matter. *Rev. Mod. Phys.* **89**, 040502 (2017).

[4] Wen, X.-G. Colloquium: Zoo of quantum-topological phases of matter. *Rev. Mod. Phys.* **89**, 041004 (2017).

[5] Ryu, S., Schnyder, A. P., Furusaki, A. & Ludwig, A. W. Topological insulators and superconductors: tenfold way and dimensional hierarchy. *New Journal of Physics* **12**, 065010 (2010).

[6] Hasan, M. Z. & Kane, C. L. Colloquium: Topological insulators. *Rev. Mod. Phys.* **82**, 3045–3067 (2010).

[7] Asbóth, J. K., Oroszlány, L. & Pályi, A. A short course on topological insulators. *Lecture notes in physics* **919**, 997–1000 (2016).

[8] Bernevig, B. A. *Topological insulators and topological superconductors* (Princeton university press, 2013).

[9] Su, W. P., Schrieffer, J. R. & Heeger, A. J. Solitons in polyacetylene. *Phys. Rev. Lett.* **42**, 1698–1701 (1979).

[10] Su, W. P., Schrieffer, J. R. & Heeger, A. J. Soliton excitations in polyacetylene. *Phys. Rev. B* **22**, 2099–2111 (1980).

[11] Bansil, A., Lin, H. & Das, T. Colloquium: Topological band theory. *Rev. Mod. Phys.* **88**, 021004 (2016).

[12] Meier, E. J., An, F. A. & Gadway, B. Observation of the topological soliton state in the su-schrieffer-heeger model. *Nature communications* **7**, 13986 (2016).

[13] St-Jean, P. *et al.* Lasing in topological edge states of a one-dimensional lattice. *Nature Photonics* **11**, 651–656 (2017).

[14] Lee, C. H. *et al.* Topolectrical circuits. *Communications Physics* **1**, 39 (2018).

[15] Wang, Y., Lang, L.-J., Lee, C. H., Zhang, B. & Chong, Y. Topologically enhanced harmonic generation in a nonlinear transmission line metamaterial. *Nature communications* **10**, 1–7 (2019).

[16] Downing, C. A., Sturges, T. J., Weick, G., Stobińska, M. & Martín-Moreno, L. Topological phases of polaritons in a cavity waveguide. *Phys. Rev. Lett.* **123**, 217401 (2019).

[17] Lee, C. H., Li, G., Jin, G., Liu, Y. & Zhang, X. Topological dynamics of gyroscopic and floquet lattices from newton's laws. *Phys. Rev. B* **97**, 085110 (2018).

[18] Kitaev, A. Y. Unpaired majorana fermions in quantum wires. *Physics-Uspekhi* **44**, 131 (2001).

[19] Verresen, R., Moessner, R. & Pollmann, F. One-dimensional symmetry protected topological phases and their transitions. *Phys. Rev. B* **96**, 165124 (2017).

[20] Leumer, N., Marganska, M., Muralidharan, B. & Grifoni, M. Exact eigenvectors and eigenvalues of the finite kitaev chain and its topological properties. *Journal of Physics: Condensed Matter* **32**, 445502 (2020).

[21] Jiang, L. *et al.* Majorana fermions in equilibrium and in driven cold-atom quantum wires. *Phys. Rev. Lett.* **106**, 220402 (2011).

[22] Lobos, A. M., Lutchyn, R. M. & Das Sarma, S. Interplay of disorder and interaction in majorana quantum wires. *Phys. Rev. Lett.* **109**, 146403 (2012).

[23] Aasen, D. *et al.* Milestones toward majorana-based quantum computing. *Physical Review X* **6**, 031016 (2016).

[24] van Zanten, D. M. *et al.* Photon-assisted tunnelling of zero modes in a majorana wire. *Nature Physics* 1–6 (2020).

[25] Bagrets, D. & Altland, A. Class d spectral peak in majorana quantum wires. *Phys. Rev. Lett.* **109**, 227005 (2012).

[26] Li, L., Yang, C. & Chen, S. Winding numbers of phase transition points for one-dimensional topological systems. *EPL (Europhysics Letters)* **112**, 10004 (2015).

[27] Li, L., Xu, Z. & Chen, S. Topological phases of generalized su-schrieffer-heeger models. *Phys. Rev. B* **89**, 085111 (2014).

[28] Schnyder, A. P., Ryu, S., Furusaki, A. & Ludwig, A. W. W. Classification of topological insulators and superconductors in three spatial dimensions. *Phys. Rev. B* **78**, 195125 (2008).

[29] Lee, C. H., Li, L., Thomale, R. & Gong, J. Unraveling non-hermitian pumping: Emergent spectral singularities and anomalous responses. *Phys. Rev. B* **102**, 085151 (2020).

[30] Li, L., Lee, C. H. & Gong, J. Geometric characterization of non-hermitian topological systems through the singularity ring in pseudospin vector space. *Phys. Rev. B* **100**, 075403 (2019).

[31] García-Pérez, G., Rossi, M. A. & Maniscalco, S. Ibm q experience as a versatile experimental testbed for simulating open quantum systems. *npj Quantum Information* **6**, 1–10 (2020).

[32] Cross, A. The ibm q experience and qiskit open-source quantum computing software. In *APS March Meeting Abstracts*, vol. 2018, L58–003 (2018).

[33] Andersson, S. *et al.* Learn quantum computation using qiskit (2020). URL http://community.qiskit.org/textbook.

[34] Aleksandrowicz, G. *et al.* Qiskit: An Open-source Framework for Quantum Computing (2019). URL https://doi.org/10.5281/zenodo.2562111.

[35] Smith, A., Kim, M. S., Pollmann, F. & Knolle, J. Simulating quantum many-body dynamics on a current digital quantum computer. *npj Quantum Information* **5**, 106 (2019).

[36] Kandala, A. *et al.* Error mitigation extends the computational reach of a noisy quantum processor. *Nature* **567**, 491–495 (2019).

[37] Kandala, A. *et al.* Hardware-efficient variational quantum eigensolver for small molecules and quantum magnets. *Nature* **549**, 242–246 (2017).

[38] Temme, K., Bravyi, S. & Gambetta, J. M. Error mitigation for short-depth quantum circuits. *Phys. Rev. Lett.* **119**, 180509 (2017).

[39] Alvarez-Rodriguez, U., Sanz, M., Lamata, L. & Solano, E. Quantum artificial life in an ibm quantum computer. *Scientific Reports* **8**, 14793 (2018).

[40] Behera, B. K., Reza, T., Gupta, A. & Panigrahi, P. K. Designing quantum router in ibm quantum computer. *Quantum Information Processing* **18**, 328 (2019).

[41] McCaskey, A. J. *et al.* Quantum chemistry as a benchmark for near-term quantum computers. *npj Quantum Information* **5**, 99 (2019).

[42] Zhukov, A. A., Remizov, S. V., Pogosov, W. V. & Lozovik, Y. E. Algorithmic simulation of far-from-equilibrium dynamics using quantum computer. *Quantum Information Processing* **17**, 223 (2018).

[43] Sun, S.-N. *et al.* Quantum computation of finite-temperature static and dynamical properties of spin systems using quantum imaginary time evolution. *PRX Quantum* **2**, 010317 (2021).

[44] Motta, M. *et al.* Determining eigenstates and thermal states on a quantum computer using quantum imaginary time evolution. *Nature Physics* **16**, 205–210 (2020).

[45] Georgescu, I. M., Ashhab, S. & Nori, F. Quantum simulation. *Rev. Mod. Phys.* **86**, 153–185 (2014).

[46] Ortiz, G., Gubernatis, J. E., Knill, E. & Laflamme, R. Quantum algorithms for fermionic simulations. *Phys. Rev. A* **64**, 022319 (2001).

[47] Somma, R., Ortiz, G., Gubernatis, J. E., Knill, E. & Laflamme, R. Simulating physical phenomena by quantum networks. *Phys. Rev. A* **65**, 042323 (2002).

[48] Nielsen, M. A. & Chuang, I. L. *Quantum Computation and Quantum Information* (Cambridge University Press, The Edinburgh Building, Cambridge CB2 8RU, UK, 2000).

[49] Cross, A. W., Bishop, L. S., Sheldon, S., Nation, P. D. & Gambetta, J. M. Validating quantum computers using randomized model circuits. *Phys. Rev. A* **100**, 032328 (2019).

[50] Moll, N. *et al.* Quantum optimization using variational algorithms on near-term quantum devices. *Quantum Science and Technology* **3**, 030503 (2018).

[51] Kraus, B. & Cirac, J. I. Optimal creation of entanglement using a two-qubit gate. *Phys. Rev. A* **63**, 062309 (2001).

[52] Vatan, F. & Williams, C. Optimal quantum circuits for general two-qubit gates. *Phys. Rev. A* **69**, 032315 (2004).

[53] Drury, B. & Love, P. Constructive quantum shannon decomposition from cartan involutions. *Journal of Physics A: Mathematical and Theoretical* **41**, 395305 (2008).

[54] Möttönen, M., Vartiainen, J. J., Bergholm, V. & Salomaa, M. M. Quantum circuits for general multiqubit gates. *Phys. Rev. Lett.* **93**, 130502 (2004).

[55] Vartiainen, J. J., Möttönen, M. & Salomaa, M. M. Efficient decomposition of quantum gates. *Phys. Rev. Lett.* **92**, 177902 (2004).

[56] Khaneja, N. & Glaser, S. J. Cartan decomposition of su (2n) and control of spin systems. *Chemical Physics* **267**, 11–23 (2001).

[57] Vogel, K. & Risken, H. Determination of quasiprobability distributions in terms of probability distributions for the rotated quadrature phase. *Phys. Rev. A* **40**, 2847–2849 (1989).

[58] James, D. F., Kwiat, P. G., Munro, W. J. & White, A. G. On the measurement of qubits. In *Asymptotic Theory of Quantum Statistical Inference: Selected Papers*, 509–538 (World Scientific, 2005).

[59] Lvovsky, A. I. & Raymer, M. G. Continuous-variable optical quantum-state tomography. *Rev. Mod. Phys.* **81**, 299–332 (2009).

[60] Garcia-Escartin, J. C. & Chamorro-Posada, P. swap test and hong-ou-mandel effect are equivalent. *Phys. Rev. A* **87**, 052330 (2013).

[61] Kang, M.-S., Heo, J., Choi, S.-G., Moon, S. & Han, S.-W. Implementation of swap test for two unknown states in photons via cross-kerr nonlinearities under decoherence effect. *Scientific reports* **9**, 1–14 (2019).

[62] Whitfield, J. D., Biamonte, J. & Aspuru-Guzik, A. Simulation of electronic structure hamiltonians using quantum computers. *Molecular Physics* **109**, 735–750 (2011).

[63] Aspuru-Guzik, A., Dutoi, A. D., Love, P. J. & Head-Gordon, M. Simulated quantum computation of molecular energies. *Science* **309**, 1704–1707 (2005).

[64] Cleve, R., Ekert, A., Macchiavello, C. & Mosca, M. Quantum algorithms revisited. *Proceedings of the Royal Society of London. Series A: Mathematical, Physical and Engineering Sciences* **454**, 339–354 (1998).

[65] Dobšíček, M., Johansson, G., Shumeiko, V. & Wendin, G. Arbitrary accuracy iterative quantum phase estimation algorithm using a single ancillary qubit: A two-qubit benchmark. *Phys. Rev. A* **76**, 030306 (2007).

[66] Mohammadbagherpoor, H. *et al.* An improved implementation approach for quantum phase estimation on quantum computers. In *2019 IEEE International Conference on Rebooting Computing (ICRC)*, 1–9 (IEEE, 2019).

[67] Seeley, J. T., Richard, M. J. & Love, P. J. The bravyi-kitaev transformation for quantum computation of electronic structure. *The Journal of chemical physics* **137**, 224109 (2012).

[68] Vidal, G. Efficient simulation of one-dimensional quantum many-body systems. *Phys. Rev. Lett.* **93**, 040502 (2004).

[69] Trotter, H. F. On the product of semi-groups of operators. *Proceedings of the American Mathematical Society* **10**, 545–551 (1959).

[70] Sieberer, L. M. *et al.* Digital quantum simulation, trotter errors, and quantum chaos of the kicked top. *npj Quantum Information* **5**, 1–11 (2019).

[71] Heyl, M., Hauke, P. & Zoller, P. Quantum localization bounds trotter errors in digital quantum simulation. *Science advances* **5**, eaau8342 (2019).

[72] Hatano, N. & Suzuki, M. *Finding Exponential Product Formulas of Higher Orders*, 37–68 (Springer Berlin Heidelberg, Berlin, Heidelberg, 2005).

[73] Khatri, S. *et al.* Quantum-assisted quantum compiling. *Quantum* **3**, 140 (2019).
[74] Jones, T. & Benjamin, S. C. Quantum compilation and circuit optimisation via energy dissipation. *arXiv preprint arXiv:1811.03147* (2020).
[75] Heya, K., Suzuki, Y., Nakamura, Y. & Fujii, K. Variational quantum gate optimization. *arXiv preprint arXiv:1810.12745* (2018).
[76] Gray, J. quimb: A python package for quantum information and many-body calculations. *Journal of Open Source Software* **3**, 819 (2018).
[77] Andrew, G. & Gao, J. Scalable training of l1-regularized log-linear models. In *International Conference on Machine Learning* (2007).
[78] Malouf, R. A comparison of algorithms for maximum entropy parameter estimation. In *Proceedings of the 6th Conference on Natural Language Learning*, vol. 20 of *COLING-02*, 1–7 (Association for Computational Linguistics, USA, 2002).
[79] IBM Quantum (2021). URL https://quantum-computing.ibm.com/.
[80] McArdle, S., Yuan, X. & Benjamin, S. Error-mitigated digital quantum simulation. *Phys. Rev. Lett.* **122**, 180501 (2019).